A Gamma-Ray Flare from TXS 1508+572

Characterizing the Jet of a z = 4.31 Blazar in the Early Universe

Gokus, Andrea; Böttcher, Markus; Errando, Manel; Kreter, Michael; Heßdörfer, Jonas; Eppel, Florian; Kadler, Matthias; Smith, Paul S.; Gurvits, Leonid I.; More Authors

Important note
To cite this publication, please use the final published version (if applicable).
Please check the document version above.

A Gamma-Ray Flare from TXS 1508+572: Characterizing the Jet of a $z = 4.31$ Blazar in the Early Universe

Andrea Gokus[1] , Markus Böttcher[2] , Manel Errando[1] , Michael Kreter[2] , Jonas Heßdörfer[3] , Florian Eppel[3] ,
Matthias Kadler[3] , Paul S. Smith[4] , Petra Benke[3,5] , Leonid I. Gurvits[6,7] , Alex Kraus[5] , Mikhail Lisakov[5,8] ,
Felicia McBride[9] , Eduardo Ros[5] , Florian Rösch[3,5] , and Jörn Wilms[10]

[1] Department of Physics & McDonnell Center for the Space Sciences, Washington University in St. Louis, One Brookings Drive, St. Louis, MO 63130, USA;
gokus@wustl.edu
[2] Centre for Space Research, North-West University, Potchefstroom 2520, South Africa
[3] Julius-Maximilians-Universität Würzburg, Fakultät für Physik und Astronomie, Institut für Theoretische Physik und Astrophysik, Lehrstuhl für Astronomie, Emil-Fischer-Str. 31, D-97074 Würzburg, Germany
[4] Steward Observatory, The University of Arizona, Tucson, AZ 85721, USA
[5] Max-Planck-Institut für Radioastronomie, Auf dem Hügel 69, D-53121 Bonn, Germany
[6] Joint Institute for VLBI ERIC (JIVE), Oude Hoogeveensedijk 4, 7991 PD, Dwingeloo, The Netherlands
[7] Faculty of Aerospace Engineering, Delft University of Technology, Kluyverweg 1, 2629 HS, Delft, The Netherlands
[8] Instituto de Física, Pontificia Universidad Católica de Valparaíso, Casilla 4059, Valparaíso, Chile
[9] Department of Physics and Astronomy, Bowdoin College, Brunswick, ME 04011, USA
[10] Remeis Observatory & Erlangen Centre for Astroparticle Physics, Universität Erlangen-Nürnberg, Sternwartstr. 7, 96049 Bamberg, Germany
Received 2024 May 28; revised 2024 July 22; accepted 2024 July 30; published 2024 October 3

Abstract

Blazars can be detected from very large distances due to their high luminosity. However, the detection of γ-ray emission of blazars beyond $z = 3$ has only been confirmed for a small number of sources. Such observations probe the growth of supermassive black holes close to the peak of star formation in the history of galaxy evolution. As a result from a continuous monitoring of a sample of 80 $z > 3$ blazars with the Fermi Large Area Telescope (Fermi-LAT), we present the first detection of a γ-ray flare from the $z = 4.31$ blazar TXS 1508+572. This source showed high γ-ray activity from 2022 February to August, reaching a peak luminosity comparable to the most luminous flares ever detected with Fermi-LAT. We conducted a multiwavelength observing campaign involving XMM-Newton, the Neil Gehrels Swift Observatory, the Effelsberg 100 m radio telescope, and the Very Long Baseline Array. In addition, we make use of the monitoring programs by the Zwicky Transient Facility and the Near-Earth Object Wide-field Infrared Survey Explorer at optical and infrared wavelengths, respectively. We find that the source is particularly variable in the infrared band on daily timescales. The spectral energy distribution collected during our campaign is well described by a one-zone leptonic model, with the γ-ray flare originating from an increase of external Compton emission as a result of a fresh injection of accelerated electrons.

Unified Astronomy Thesaurus concepts: Blazars (164); Gamma-ray astronomy (628); Relativistic jets (1390);
Radiative processes (2055); High energy astrophysics (739); High-redshift galaxies (734); Flat-spectrum radio
quasars (2163)

Materials only available in the online version of record: data behind figures

1. Introduction

Among jetted active galactic nuclei (AGN), those with their jet pointing toward the Earth are called blazars and appear particularly variable and luminous due to relativistic beaming (Urry & Padovani 1995). Blazars can be broadly classified as either BL Lacertae objects (BL Lac objects) or flat-spectrum radio quasars (FSRQs), for which the distinction is based on the existence of optical emission lines with an equivalent width of at least 5 Å (FSRQ) or the lack thereof (BL Lac objects).

Due to their extreme luminosities, we are able to detect quasars and blazars at large distances, currently up to $z = 7.6$ (Wang et al. 2021), which enables glimpses into the early Universe. Among those found at high redshift, some seem to be powered by the heaviest specimens of black holes, exceeding a billion solar masses (e.g., Lobanov et al. 2001; Ghisellini et al. 2010; Ackermann et al. 2017; Belladitta et al. 2022; Burke

et al. 2024). Given that these extremely massive black holes appear to exist only about one billion years after the Big Bang, the circumstances under which black holes can grow so fast are not yet understood (see, e.g., Inayoshi et al. 2020, for a recent review). While our observations are biased toward finding the most luminous and therefore extreme sources, current estimations for their number densities present a hurdle for the application of our existing models that describe black hole formation and growth (e.g., Johnson & Haardt 2016). Some of the suggestions for black hole formation for heavy seeds are remnants of the supernovae of massive first-generation stars (Madau & Rees 2001), or matter collapsing into supermassive black holes (SMBHs) right away (e.g., Begelman et al. 2006). However, even with black hole seeds of $\sim100\ M_\odot$ the timescales needed for SMBHs to grow to $>10^9\ M_\odot$ are too long even when assuming accretion at the Eddington limit throughout the entire time. Work by Volonteri et al. (2011) and Ghisellini et al. (2013) investigate the role of AGN feedback in relation to black hole growth and propose a scenario in which powerful jets can prompt a higher accretion rate. Alexander & Natarajan (2014) have suggested that the first black holes might

have been able to grow fast through supraexponential accretion. A recent study by Lai et al. (2024) argues that SMBHs at $z \sim 5$ are only growing slowly, thereby requiring either initial seed masses $> 10^8 \, M_\odot$ or extremely rapid growth at $z > 5$. Simulations of rapidly spinning black holes accreting above the Eddington limit have revealed that their growth is accompanied by the formation of powerful jets (McKinney et al. 2014; Sądowski et al. 2014). Hence, high-redshift ($z > 3$) blazars are ideal targets in order to learn more about the growth of SMBHs, while also taking into account that their powerful large-scale jets influence their host galaxies and galaxy clusters, which affect galaxy evolution.

In order to properly assess the physical properties of these blazars, it is essential to obtain a multiwavelength data set for these objects, in particular, information about the high-energy emission that is needed to measure the full power of the jet. While at X-ray energies we have been able to probe distances up to $z > 6$ (e.g., Sbarrato et al. 2015; Belladitta et al. 2020; Medvedev et al. 2020; Sbarrato et al. 2022; Migliori et al. 2023), we have not been able to do so at γ-ray energies, even though the Universe is transparent up to 10 GeV (Domínguez et al. 2024). However, due to both the large distance and the shift of the emitted γ-ray emission to lower energies where the sensitivity of the Fermi Large Area Telescope (Fermi-LAT) decreases, most of the blazars appear to be too faint to be detected. Studies on high-z blazars are currently limited to a small sample of objects with $z \geqslant 3$. The current version of the AGN catalog based on data from Fermi-LAT lists 11 blazars (Ajello et al. 2020, 2022), and other studies have identified three more high-z blazars (Liao et al. 2018; Kreter et al. 2020).

A blazar's broadband spectral energy distribution (SED) consists of two broad, nonthermal components, where the low-energy component can be generally attributed to leptonic synchrotron emission, while the high-energy component can be explained by leptonic inverse Compton (IC) processes (e.g., Maraschi et al. 1992; Dermer & Schlickeiser 1993; Sikora et al. 1994; Blandford & Levinson 1995; Bloom & Marscher 1996; Boettcher & Schlickeiser 1997; Błażejowski et al. 2000), but also additional hadronic interactions such as photon–pion interactions and proton synchrotron emission (e.g., Mannheim & Biermann 1992; Mannheim 1993; Aharonian 2000; Mücke & Protheroe 2001; Aharonian 2002; Mücke et al. 2003; Böttcher et al. 2013). In addition, some blazars feature a thermal component from their accretion disks, which are particularly present in high-z sources for which the emission from the disk is redshifted to optical and even IR wavelengths. As the entire emission from high-z blazars becomes redshifted, the peak of the high-energy component drifts to MeV energies, which led to the term "MeV blazar" being coined (Bloemen et al. 1995). In addition, Sikora et al. (2002) have also presented an underlying physical distinction from GeV blazars that relates to electron cooling through Comptonization of near-infrared emission from the dusty torus in the case of MeV blazars. As a result, the γ-ray spectra of these objects are steep (Ackermann et al. 2017).

In Section 2, we outline our strategy of detecting γ-ray flares from high-z blazars and introduce TXS 1508+572. Our data reduction is described in Section 3. We compute the γ-ray luminosity displayed by TXS 1508+572 during its peak in Section 4.1 and assess the changes in the γ-ray, X-ray, and radio spectra in Section 4.2. In addition, our results of the multiwavelength data analysis include a variability study of

TXS 1508+572 during the flaring state as well as some long-term variability in Section 4.3 and a modeling of the broadband SED in Section 4.4. Finally, we discuss all our findings and conclude in Section 5. Throughout this paper, we assume a flat cosmology following Planck Collaboration et al. (2016), who reported $H_0 = 67.8 \, \mathrm{km \, s^{-1}}$, $\Omega_\Lambda = 0.692$, and $\Omega_M = 0.308$. With those parameters, TXS 1508+572 has a luminosity distance of ~ 40 Gpc.

2. Monitoring Campaign

While several studies have been collecting multiwavelength data for MeV blazars and have modeled their SEDs using non- or semicontemporaneous data (e.g., Paliya et al. 2016; Ackermann et al. 2017; Marcotulli et al. 2020), some have reported on the analysis of flares from high-z blazars using quasi-simultaneous data sets (albeit some sources with $2 < z < 3$; Orienti et al. 2014; Liao et al. 2019; Paliya et al. 2019). In order to be able to catch a high-z blazar during a γ-ray flare, we use Fermi-LAT's all-sky monitoring capabilities and set up a γ-ray monitoring program for 80 sources for which the fifth version of the ROMA-BZCAT (Massaro et al. 2009, 2015) lists as being at $z > 3$. Our method relies on a significant detection (i.e., a test statistic (TS) $\geqslant 25$, where $\mathrm{TS} = 2\Delta \log(\mathcal{L})$ compares the likelihood with and without a source; see Section 3.1 for details) for 30 day average time bins, for which we perform a daily check. Using 30 day average time bins has been proven successful in the search for high-z blazars using archival data (Kreter et al. 2020).

In order to obtain a simultaneous multiwavelength data set upon flare detection, we set up follow-up observations using multiple facilities (100 m Effelsberg radio telescope, XMM-Newton, and the Neil Gehrels Swift Observatory (Swift)) and also make use of existing all-sky survey facilities such as the Zwicky Transient Facility (ZTF) and the Near-Earth Object Wide-field Infrared Survey Explorer (NEOWISE).

In this work, we report on the first γ-ray flare detected for a $z > 4$ blazar, TXS 1508+572, which occurred in 2022 February and marked the beginning of a high-activity phase lasting roughly 6 months.

2.1. TXS 1508+572

At a redshift of $z = 4.31$ (Schneider et al. 2007; but note that the first report of its redshift at $z = 4.30$ was done by Hook et al. 1995), the blazar TXS 1508+572 is the third most distant γ-ray source detected with Fermi-LAT data as reported by Liao et al. (2018) and Kreter et al. (2020; but note that in the most recent release of the Fermi-LAT AGN Catalog by Ajello et al. 2022, it is still listed as the most distant γ-ray emitter). As a γ-ray emitter, the source is known as 4FGL J1510.1+5702, but historically has been referred to as GB 1508+5714. The source was first studied at X-ray energies with Einstein data (Mathur & Elvis 1995), and subsequently studied by ASCA (Moran & Helfand 1997). Using Chandra's high-resolution ACIS detector, Siemiginowska et al. (2003) and Yuan et al. (2003) independently reported on the identification of an X-ray jet seen as extended emission from the source. The first very long baseline interferometry (VLBI) high-resolution image, taken with the European VLBI Network at 5 GHz with an angular resolution of ~ 5 mas in 1995, did not reveal any extended radio emission (Frey et al. 1997). However, Very Large Array snapshot observations taken at 1.4 GHz were able to detect a

low-brightness jet extending to $\sim2\overset{''}{.}5$ toward the southwest (Cheung 2004). O'Sullivan et al. (2011) reported an optically thin jet component at 5 and 8.4 GHz roughly 2 mas to the south of the core based on global VLBI polarimetry observations. A recent observation of the source with LOFAR revealed emission from the counterjet seen at 144 MHz with subarcsecond spatial resolution (Kappes et al. 2022). On milliarcsecond scales, Titov et al. (2023) monitored TXS 1508 +572 over 4 years at 2.3 and 8.4 GHz in order to study the apparent absolute astrometric proper motion and detected a jet proper motion of 0.117 ± 0.078 mas yr^{-1}.

In 2017, the object was confirmed as a γ-ray emitter (Ackermann et al. 2017), and variability on monthly timescales has been detected (Li et al. 2018). A period of enhanced brightness in both the γ-ray and the optical bands has been reported by Liao et al. (2020).

On 2022 February 4, we detected a γ-ray flare from TXS 1508+572 through our Fermi-LAT monitoring pipeline and found that the source had significantly brightened compared to the flux reported in the Fermi-LAT Fourth Source Catalog (4FGL; Abdollahi et al. 2020; Gokus et al. 2022). We coordinated a multiwavelength campaign to obtain simultaneous data during the flaring state, and in addition launched a VLBI monitoring campaign using the Very Long Baseline Array (VLBA) and the 100 m Effelsberg radio telescope, whose results we report in Benke et al. (2024).

3. Multiwavelength Data

In this section, we report on the broadband data extraction and analysis, and show the fluxes, magnitudes, and flux densities that have been compiled in light curves for different energy bands in Figure 1.

3.1. Fermi-LAT

LAT on board the Fermi satellite (Atwood et al. 2009) has monitored the entire sky since 2008 August, and has detected 3814 AGN in 12 yr (Ajello et al. 2020, 2022), with the large majority being blazars. We extract the LAT data using ScienceTools Version 1.2.23 and fermipy 0.20.0 (Wood et al. 2017), following the standard data reduction process. Events with an energy between 100 MeV and 300 GeV are selected within a region of interest (ROI) of $15°$ around the γ-ray source coordinates given in 4FGL (Abdollahi et al. 2020), and filtered by selecting SOURCE class events and those fulfilling `DATA_QUAL > 0` and `LAT_CONFIG == 1`. In addition, we use only events that enter the instrument with a maximum zenith angle of $90°$ to avoid contamination by γ-rays from Earth-limb effects. To model the background, we use `gll_iem_v07` as the Galactic diffuse model, and `iso_-P8R3_SOURCE_V2_v1` to account for the isotropic diffusion emission. Furthermore, we use the postlaunch instrument response function `P8R3_SOURCE_V2`. In addition to the background, we include all known γ-ray sources listed in the 4FGL that lie within $20°$ of TXS 1508+572, and use the spectral type listed in the 4FGL as a model for each source. In the case of our target source, this model is represented by a power law. Optimization of our model parameters is done via a maximum likelihood analysis, for which the significance of the γ-ray emission for each source is determined via TS = $2\Delta \log(\mathcal{L})$. The likelihood function $\mathcal{L}$ describes the difference between a model with and without a source at the

given coordinates (Mattox et al. 1996). After an initial fit of all components within the ROI, we remove point sources that are found with TS < 4 or TS = NaN as their background contribution is minimal to nonexistent. By checking the resulting TS maps, we ensure that no excess emission is left over after the fitting procedure.

The γ-ray spectra of TXS 1508+572 are created for the quiescent and flaring states, which cover a time range of MJD 55197 to 59215 (2010 January 1 to 2021 January 1), and MJD 59610 to 59624 (2022 January 31 to 2022 February 14), respectively. In the spectral fits, we keep the spectral and normalization parameters free for our target source and all sources within $3°$ of it, which are initially five sources in the first fit that were all kept for the quiescent state, but removed for the fit of the flaring state. For sources within $5°$, or with TS > 500, we leave the normalization free to vary. Galactic and isotropic diffuse emissions are also kept free during the modeling.

Moreover, we compute a light curve from MJD 59434 to 60094 (2021 August 8 to 2023 May 30) with 30 day binning, and MJD 59582 to MJD 60051 (2022 January 3 to 2023 April 17) with 7 day binning, which are shown in the top two panels of Figure 1 for the 30 day and 7 day binning, respectively. The 30 day binning is chosen such that the first TS $\geqslant 25$ bin coincides with the detection of increased activity with our pipeline, i.e., on 2022 February 4. We keep the normalization free for all sources within $3°$ of TXS 1508+572, as well as sources with TS > 500 over the entire time range. In addition, we keep the spectral index of our target source as a free parameter. All diffuse emission is kept frozen to the best-fit parameters determined in the modeling of the entire time range. We display the 2σ upper limit for bins with TS < 25 for the 30 day binned light curve, and TS < 9 for the 7 day binned light curve, which equates to a detection significance of $\sim5\sigma$ and $\sim3\sigma$, respectively. The uncertainties of the flux bins are given as 1σ uncertainties.

3.2. X-Ray Data

We model all X-ray data using the Interactive Spectral Interpretation System (ISIS; version 1.6.2-51; Houck & Denicola 2000) in order to determine the spectral parameters and the source flux and utilize the C-statistics (Cash 1979). Uncertainties are given at the 1σ confidence level. The absorption by the interstellar medium is based on the `vern` cross sections (Verner et al. 1996) and the `wilm` abundances (Wilms et al. 2000). For each spectrum, we use an absorbed, pegged power law (`tbabs`*`pegpwrlw`), except for a simultaneous fit of XMM-Newton and NuSTAR spectra, which we utilize to test for a spectral break. We freeze the Galactic hydrogen absorption to the value from the H I 4π survey (HI4PI Collaboration et al. 2016), which is $N_{H, Gal} = 1.55 \times 10^{20}$ cm^{-2}. The results from our X-ray spectral fits are presented in Section 4.2. The fluxes measured with XMM-Newton and Swift and obtained from the respective best fits are shown in the third panel from the top in Figure 1.

3.2.1. XMM-Newton

We obtained a target-of-opportunity observation with the XMM-Newton observatory (Jansen et al. 2001) to follow up the flare as soon as possible after the detection of the γ-ray flare. TXS 1508+572 was observed on 2022 February 8
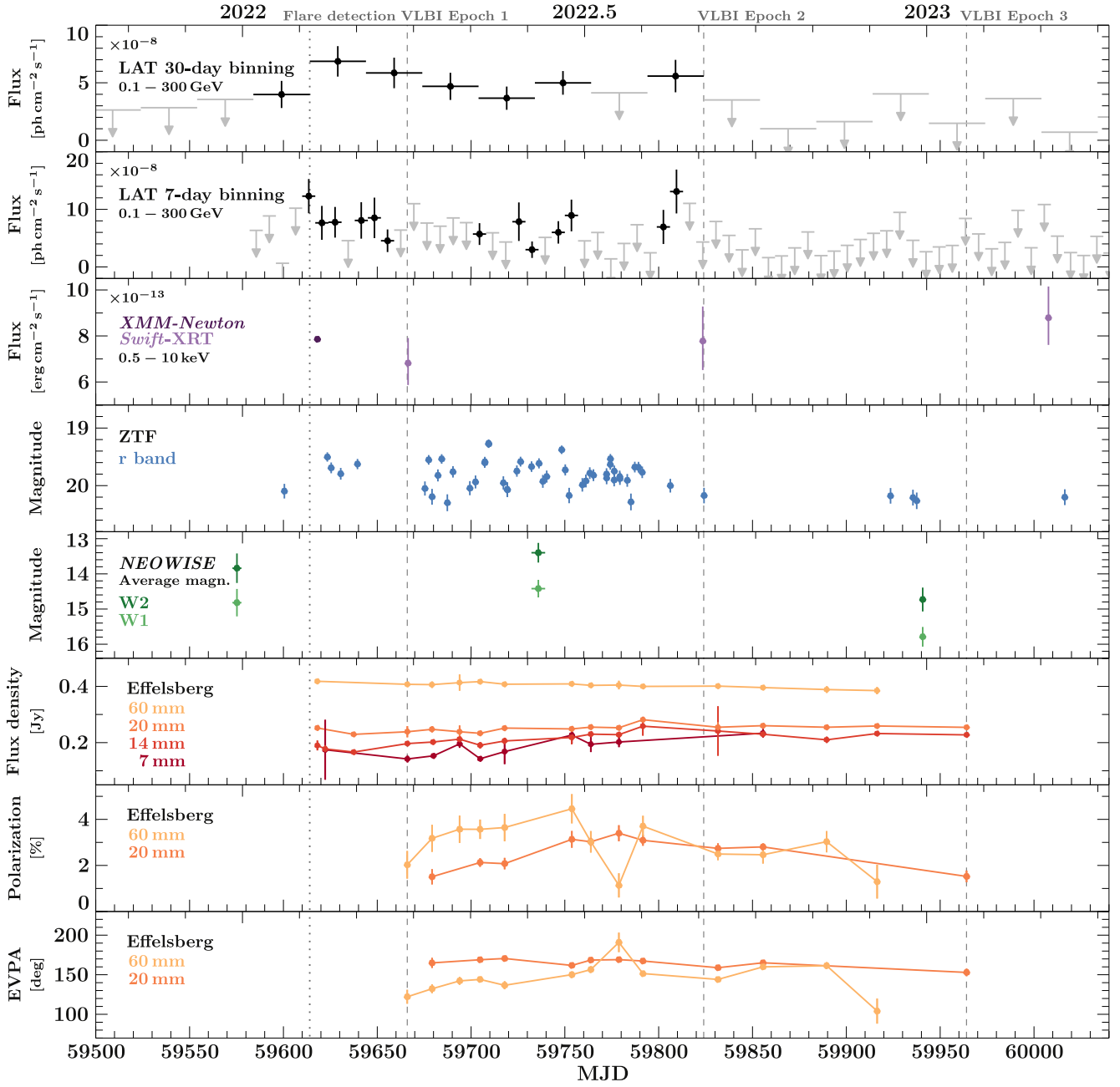
Figure 1. Multiwavelength light curve of TXS 1508+572 covering a time span from the end of 2021 to the beginning of 2023. The panels from top to bottom show the fluxes, magnitudes, and flux densities in different, decreasing energy ranges, starting with γ-rays at the top. The two bottom panels illustrate changes in the single-dish radio polarization and electric vector polarization angle (EVPA), respectively, measured at 60 mm and 20 mm. A dotted line marks the detection of the flaring state of TXS 1508+572, while the three dashed lines mark the VLBI observations presented in Benke et al. (2024).

(ObsID 0910390101) for 85 ks in the Small Window mode with the European Photon Imaging Camera (EPIC) with the pn (Strüder et al. 2001) and both MOS detectors (Turner et al. 2001). In addition, we extract the data from an archival observation performed on 2002 May 11 (ObsID 0111260201), which was taken in Full Window mode with an exposure time of 24 ks. For the archival data, we were only able to obtain spectra from the EPIC-pn and EPIC-MOS2 detectors since the source region coincides with a CCD gap for the EPIC-MOS1 detector. We extract spectra for both observations using the XMM-Newton Science Analysis Software (SAS; version 20.0.0) by using the standard methods in order to process the observation data files and produce calibrated event lists and images. The circular source regions in each detector are centered on the point source at the source coordinates with a radius of 35″ for the EPIC-pn detector as well as the EPIC-MOS2 detector for ObsID 0111260201, and a radius of 27.″5 for all other EPIC-MOS detectors. The background regions are circles positioned in a source-free region at sufficient distance from the target source, and have a radius of 60″ for all detectors except for the EPIC-MOS2 detector in ObsID 0111260201, for which we have chosen 100″. We extract single and double events for the data taken with EPIC-pn, and all events for data taken with the EPIC-MOS detectors. In both observations, pileup is negligible. We extract light curves of the observation in three different energy bands using the EPIC-pn detector: for the full energy range from 0.3 to 10 keV, as well as for the soft band from 0.3 to 2 keV and for the hard band from 2 to 10 keV.

We find that at the beginning and end of the observation, the data are impacted by severe background flaring and exclude those time ranges from any data analyses. For the remaining time range, we compute a subtracted light curve by subtracting the background light curve from the light curve obtained for the source region. To correct for detector and scaling effects, we only work with light curves produced with the XMM SAS function `epiclccorr`. Note that we also exclude all bins with a fractional exposure below 65%.

3.2.2. Neil Gehrels Swift Observatory

We requested several observations with Swift (Gehrels et al. 2004) over the course of a year, to gather contemporaneous data to the VLBI monitoring with VLBA and the 100 m Effelsberg radio telescope (Benke et al. 2024). In addition to the observations obtained in relation to the γ-ray flare, an archival observation of TXS 1508+572 exists, which was taken simultaneous to a NuSTAR observation in 2017. We use those data for creating a γ-ray quiescent-state SED of the source. The Swift X-Ray Telescope (Swift-XRT) data are extracted using the standard procedures with the `xrtpipeline` (version 0.13.7) with HEASOFT 6.30. The source spectra are compiled from the source coordinates (R.A. = 227°.5114780, decl. = 57°.0447472) and a radius of 30″, while the background is created using an annulus centered on the same coordinates, with an inner radius of 40″ and an outer radius of 150″.

We do not detect TXS 1508+572 with the optical/UV telescope on board Swift.

3.2.3. NuSTAR

We utilize an archival NuSTAR observation taken on 2017 April 30 (ObsID 60201013002), with an exposure time of 73 ks, to obtain hard X-ray data for the quiescent-state SED. We extract the data using the standard methods with NUSTARDAS (version 2.1.2) and CALBD version 20230124. Using nupipeline (version 0.4.9) we reduce data from both Focal Plane Modules A and B (FPMA and FPMB, respectively), and create calibrated event lists and images. We choose a circular region with a radius of 50″ at R.A. = 227°.5131365, decl. = 57°.0465406 and R.A. = 227°.5138372, decl. = 57°.0473028 for the source region in FPMA and FPMB, respectively. The background regions are chosen to be circular as well with a radius of 160″, and centered on R.A. = 227°.4806152, decl. = 57°.1443941, and R.A. = 227°.4856466, decl. = 57°.1484921 for FPMA and FPMB, respectively. After the data extraction, the resulting spectra have an exposure time of ∼37 ks.

3.3. Optical and Infrared Archival Data

Through Lyα (1215.67 Å) absorption, the intergalactic medium affects the optical emission from distant sources (e.g., Gunn & Peterson 1965). With a redshift of $z = 4.31$, the optical light of TXS 1508+572 is absorbed at wavelengths starting at 6443 Å, which falls in the middle of the range of the red filters.

The optical and IR data are displayed in two middle panels of Figure 1.

3.3.1. XMM-OM

The Optical Monitor (OM) on board XMM-Newton observed TXS 1508+572 simultaneous to the X-ray band, and took images in the V, U, W1, W2, and M2 filters with a net exposure of 12 ks, 12 ks, 16 ks, 20 ks, and 16 ks, respectively. We extract the photometric information using `omichain`, which is part of the XMM-Newton SAS. The source is only detected in the V, U, and W1 bands. However, all bands are affected by Lyα absorption. We include these photometric measurements in the broadband SED for display purposes.

3.3.2. ZTF

We obtained optical data from the ZTF (Bellm et al. 2019; Masci et al. 2019; IRSA 2022) survey through their public data release (DR18). The data consist of photometric measurements in the *gri* filter system. The data taken in the *g* band are fully affected by absorption by the Lyα forest, and are not taken into account in this work. The ZTF survey data for TXS 1508+572 shown in this work cover a time range from 2018 March through 2023 February, with gaps in between epochs of dense monitoring.

3.3.3. NEOWISE

At near-infrared wavelengths, we use public data from the NEOWISE mission (Mainzer et al. 2014; NEOWISE Team 2020), in particular the 2024 data release, which includes data from 2013 December 25 up to 2023 June 6. Data are available for two wavelength bands, which are 3.4 and 4.6 μm, and we have initially selected all data available within 5″ around the source coordinates from the online database.[11] For the data selection, we have applied the following criteria (see description in Anjum et al. 2020; which follows Rakshit et al. 2019):

1. the fit quality given as the reduced χ^2 (`w1rchi2/w2rchi2`) is less than 5 in both photometric bands;
2. the number of components used to perform a profile fit (`nb`) of the point-spread function is <3; and
3. the single-exposure images exhibit the best quality (`qi_fact =1`) and are unaffected by known artifacts (`cc_flags = 0000`) and not actively deblended (`na =0`).

Additionally, we only take into account frames with the highest quality (`qual_frame =10`). In our analysis, we only use measured magnitudes, that is, magnitudes for which an uncertainty is given, but no upper limits. We note that one W2 band observation taken in 2019 December shows a magnitude of ∼12 mag for TXS 1508+572, but for the simultaneous observation in the W1 band, no significant increase is present. Hence, even though the data quality is good and an uncertainty is available for that particular observation, we exclude it, as it is likely that it is due to a spurious effect and not an extremely bright and rapid flare of TXS 1508+572.

3.3.4. Steward Observatory

TXS 1508+572 was observed on 2023 June 19 UTC with the Steward Observatory 2.3 m Bok Telescope, located on Kitt Peak, AZ, using the SPOL spectropolarimeter (Schmidt et al. 1992). The faintness of the quasar dictated that the instrument be configured to provide imaging linear polarimetry (see, e.g., Smith et al. 2007). A KPNO "nearly Mould" *I* filter was used having an effective wavelength of 820 nm and a bandpass of ∼185 nm FWHM. The filter bandpass selected corresponds to an effective wavelength of ∼154 nm and FWHM of ∼35 nm in the rest frame of the quasar. The only major spectral feature

---

[11] https://irsa.ipac.caltech.edu/cgi-bin/Gator/nph-dd

Table 1
γ-Ray Detections in Different Binnings and during the Two Brightest Time Ranges of the Long-time Flaring State, Including the Measured Fluxes and Computed Luminosities

Bin	TS	Photon Index	Flux (ph cm^{-2} s^{-1})	Luminosity (erg s^{-1})
MJD 59610−59617				
59610−59617 (7 days)	55.54	2.41 ± 0.21	$1.2 \pm 0.3 \times 10^{-7}$	$2.6 \pm 1.0 \times 10^{49}$
59610−59613 (3 days)	37.29		$1.4 \pm 0.4 \times 10^{-7}$	$2.8 \pm 1.4 \times 10^{49}$
59611−59612 (1 day)	24.99		$2.6 \pm 1.0 \times 10^{-7}$	$5.3 \pm 2.6 \times 10^{49}$
MJD 59806−59813				
59806−59813 (7 days)	35.89	2.78 ± 0.29	$1.2 \pm 0.3 \times 10^{-7}$	$3.2 \pm 1.0 \times 10^{49}$
59809−59812 (3 days)	19.16		$1.4 \pm 0.5 \times 10^{-7}$	$3.6 \pm 1.5 \times 10^{49}$
59811−59812 (1 day)	20.97		$2.6 \pm 1.0 \times 10^{-7}$	$6.8 \pm 3.0 \times 10^{49}$

Note. Fluxes and luminosities are given for the energy range from 100 MeV to 300 GeV.

expected within the bandpass is C IV $\lambda 1549$. The 9600 s observation yields $q = 0.0092 \pm 0.0161$ and $u = 0.0087 \pm 0.0163$ for the normalized linear Stokes parameters using a $6''$ circular photometric aperture centered on TXS 1508+572. As a result, only a 1σ upper limit of about 2.9% can be estimated for the object's polarization, ignoring the statistical bias associated with low-signal-to-noise linear polarization measurements.

3.4. Effelsberg 100 m Radio Telescope

We observed TXS 1508+572 over 11 months, from 2022 February to 2023 January, with the Effelsberg 100 m telescope. These observations covered a wide wavelength range in four bands, centered around 60, 20, 14, and 7 mm. We performed cross scans over the position of the point-like source in azimuth and elevation, increasing the number of repeating scans for higher frequencies to account for the lower flux densities. The data are then averaged, undergo a quality check by a semi-automatic pipeline, corrected for pointing offsets, atmospheric opacity, and elevation-dependent gain errors, and lastly calibrated using 3C 286, which is a standard calibration source. The observation and data reduction process is described in more detail in Eppel et al. (2024). We followed the same strategy, but we increased the number of scan repetitions to 32 for the highest frequencies and also included 60 mm observations. The radio light curves in the different bands are shown in the third panel from the bottom in Figure 1. For the radio spectra, we find indices of $\alpha = -0.41 \pm 0.05$, $\alpha = -0.5 \pm 0.21$, and $\alpha = -0.24 \pm 0.22$ for the spectra $S \propto \nu^{\alpha}$ between 60 mm and 20 mm, 20 mm and 14 mm, and 14 mm and 7 mm, respectively.

In addition, for frequencies in the 60 mm and 20 mm bands, we were able to perform polarization measurements during 13 epochs as well. We find an average polarization and standard deviation of $2.9 \pm 1.1\%$ and $2.6 \pm 0.9\%$ for 60 mm and 20 mm, respectively, and plot the changes of the polarization in the second panel from the bottom in Figure 1. In addition, we also observe some rotations in the electric vector polarization angle (EVPA), which are shown in the bottom panel of Figure 1.

4. Results

4.1. Maximum γ-Ray Flux

TXS 1508+572 showed prolonged γ-ray activity for over 6 months in 2022. During this period, the source exhibited flux variability on weekly timescales (Figure 1). In order to derive the maximum γ-ray flux and obtain a value for the overall isotropic γ-ray luminosity this blazar was able to produce, we compute light curves with shorter binnings that cover the two brightest bins in the 7 day binned light curve, that is, from MJD 59610 to 59616 (2023 January 31–2023 February 6), and MJD 59806 to 59812 (2023 August 15–2023 August 21). In order to compute the γ-ray luminosity from 100 MeV to 300 GeV, we use the spectral parameters obtained by modeling each 7 day time span. The results are given in Table 1. With values ranging from $(2.6–6.8) \times 10^{49}$ erg s^{-1}, TXS 1508+572 exhibits an integrated isotropic γ-ray luminosity comparable to the most luminous blazar flares reported by the Fermi-LAT mission since 2008: 3C 279 ($\sim 10^{49}$ erg s^{-1}; Ackermann et al. 2016), CTA 102 (3×10^{50} erg s^{-1}; Gasparyan et al. 2018), 3C 454.3 ($1–4 \times 10^{49}$ erg s^{-1}; Nalewajko 2013, 2017), and PKS 0402-362 (1.5×10^{49} erg s^{-1}; Nalewajko 2013).

4.2. Spectral Analysis

4.2.1. Fermi-LAT Spectra

The γ-ray spectra for both the quiescent and flaring states were modeled with a power law in the energy range from 100 MeV to 300 GeV. The best-fit results for both spectra are listed in Table 2. While for the quiescent state an integration time of 10 yr was necessary to constrain the spectral parameters well, we were able to produce a spectrum with a similarly bound photon index over an integration time of only 14 days during the flaring state. The spectrum during the flare ($\Gamma \approx 2.4$) is significantly harder than the long-term quiescent state ($\Gamma \approx 3$), and the flux is a factor of 12 larger. Flaring blazars commonly show spectral hardening compared to their time-averaged states (e.g., Gasparyan et al. 2018). Other high-z blazars have displayed this behavior as well (Li et al. 2018; Paliya et al. 2019).

4.2.2. X-Ray Spectra

All available X-ray spectra from archival and dedicated observations are fit as described in Section 3.2. Spectra taken with the different detectors on board XMM-Newton are fit simultaneously, and we also fit simultaneously NuSTAR and Swift/XRT observations that were taken together in 2017 April. During the fit procedure, we assume that the power-law index is the same across the considered full energy range and fit the flux for that entire energy range as well. In addition, we

Table 2
γ-Ray Spectral Parameters for the Quiescent and Flaring State for the Energy Range of 0.1–100 GeV, Which Are Also Used in the Broadband Spectral Energy Distribution

Parameter	Quiescent	Flare
TS	79.0	69.4
Flux [10^{-9} ph cm^{-2} s^{-1}]	8.5 ± 0.1	103 ± 22
Photon index	2.99 ± 0.13	2.36 ± 0.17
Energy flux [10^{-12} erg cm^{-2} s^{-1}]	2.7 ± 0.4	59 ± 14
L_γ [10^{48} erg s^{-1}]	2.8 ± 0.2	21 ± 7

Note. The time ranges are from 2010 January 1 to 2019 December 31 (MJD 55197–59214) for the quiescent and January 31 to 2022 February 13 (MJD 59610–59623) for the flaring state.

adopt a cross-normalization constant for the different detectors. The best-fit results are listed in Table 3, and the simultaneously fit spectra for 2002, 2017, and 2022 are plotted in Figure 2. The photon statistics obtained in the Swift observations following the γ-ray flare are insufficient to assess the presence of X-ray spectral variability. Comparing the two XMM-Newton observations, one taken in 2002 and one directly after the detection of the γ-ray flare, we find that the the X-ray flux is slightly elevated during the γ-ray flare but the spectral shape has not significantly changed. The best-fit spectral index of the combined NuSTAR and Swift/XRT spectra taken in 2017 ($\Gamma = 1.12 \pm 0.07$) is harder than the XMM-Newton spectra from 2002 and 2022, for which the spectral index can be constrained equally well. Marcotulli et al. (2020) fit the NuSTAR data set together with archival, noncontemporaneous data from Chandra and XMM-Newton (the same 2002 observation included in this work). Their simple power-law fit results in a softer spectrum than found by our fit of the NuSTAR and Swift data together. However, the Chandra and XMM-Newton data sets are able to provide much better photon statistics in the soft X-ray band than the short Swift exposure, and Marcotulli et al. (2020) report the finding of two breaks in their spectrum, which occur at 0.8 and 6 keV, and for which the spectrum softens in between these breaks to $\Gamma \sim 1.49$, but is significantly harder at lower and higher energies ($\Gamma \sim 1$). We have tested a broken power-law model to search for at least the break at 6 keV with our combined NuSTAR and Swift/XRT data set, but could not detect it, probably because the combined spectrum is dominated by photons detected with NuSTAR, for which the sensitivity only starts at 3 keV. Hence, we cannot state whether the shape of the X-ray spectrum of TXS 1508 +572 has varied over time.

4.3. Flux Variability Analysis

We assess the flux variability of TXS 1508+572 in different energy bands by computing the normalized excess variance (Nandra et al. 1997), defined as

$$\sigma_{\mathrm{RMS}}^2 = \frac{1}{N\mu^2}\sum_{i=1}^{N}[(X_i - \mu)^2 - \sigma_i^2], \qquad (1)$$

where N is the number of bins, X_i is the flux or count rate in each bin, μ is the mean flux or count rate, and σ_i is the statistical uncertainty associated with X_i. Depending on the cadence of observations, we are able to examine daily to

monthly timescales. Negative values of σ_{RMS}^2 indicate that no variability is present in addition to the expected noise.

4.3.1. Short-term Variability with XMM-Newton

The long duration of the XMM-Newton observation (>80 ks) enables us to probe intraday flux variability of TXS 1508+572 at X-ray energies. We extract binned light curves using the EPIC-pn detector with 100 s, 300 s, and 1 ks binning for the full band (0.3–10 keV) as well as in the soft (0.3–2 keV) and hard (2–10 keV) bands (see Section 3.2.1 for details). Parts of these light curves are affected by background flaring events, which we have filtered out by excluding periods where the background count rate lies above a certain threshold that depends on the energy band and binning.

We compute the normalized excess variance σ_{RMS}^2 for all binning and energy combinations. While the values of σ_{RMS}^2 for the light curves with 100 s and 300 s binning are consistent with zero (i.e., no variability detectable above the noise level) for all energy bands, the 1 ks binned light curve exhibits small source-intrinsic variability, which is strongest in the 0.3–2 keV band (see Table 4). In the hard band, the resulting σ_{RMS}^2 is consistent with zero, that is, the noise level, within the uncertainties. The 1 ks binned light curves are shown in Figure 3.

4.3.2. Flux Variability in the Optical and Infrared

At optical and IR wavelengths, we are able to probe variability at both short- and long-term timescales. Observations were conducted from 2018 until 2023 with ZTF in the optical band (see Figure 4), and from 2013 until 2023 with NEOWISE in the IR band (see Figure 5). While NEOWISE covers the W1 and W2 bands every 6 months for a few days with cadences typically ranging from 90 minutes to a few hours, the monitoring cadence with ZTF varies and depends more strongly on the filter and each year.

For both the optical and IR light curves we calculate σ_{RMS}^2 for each epoch and plot them together with the light curves in Figures 4 and 5, respectively. We only calculate σ_{RMS}^2 for epochs that contain more than five bins, which is not the case for some W2 NEOWISE epochs. The flux variability of TXS 1508+572 changes over time in both the IR and optical bands. An IR flare is observed to begin $\sim$5 weeks before we reported the detection of the γ-ray flare, peaks during the γ-ray active phase of TXS 1508+572, and gradually decreases back to baseline (see Figure 5). Due to the sparse IR data sampling every six months, we cannot determine if the IR emission leads the γ-ray emission since we do not know when the actual peak of the IR flux is reached. The strong increase in the IR flux occurs earlier than we see such a significant increase at γ-ray energies; a rise of the γ-ray flux with a similar amplitude would have likely caused a detection above our trigger threshold earlier on. However, with our flare detection relying on a significant signal over 30 days prior, one could argue that there is a slight overlap between the first significant bin in the γ-ray light curve (top panel in Figure 1) and the elevated IR flux measured about a week before we start to integrate over the γ-ray flux for the first significant bin. Hence, the start of the flaring activity could have occurred simultaneously, but with the data on hand we can neither confirm nor reject it. The short-term IR variability peaks at the onset of the IR flare and

Table 3
Best-fit Results for the X-Ray Spectra, Fitted Individually for Swift-XRT and XMM-Newton, and for NuSTAR Fitted Combined with the Simultaneous Swift-XRT Observation, Which Is Marked with an * in the List of Swift Observations

Instrument	ObsID	Date	MJD	Net Exposure (ks)	Photon Index	Flux $(10^{-12}$ erg cm^{-2} s$^{-1})$	Fit statistic vs. exp. C value and variance	Detector constant
	00081828001*	2017-04-30	57873.4	2.1	$1.17^{+0.36}_{-0.28}$	$0.78^{+0.24}_{-0.25}$	21.5 / 26.3 $\pm$ 5.9	⋯
	00015096001	2022-03-28	59666.4	9.9	1.55 ± 0.17	$0.68^{+0.11}_{-0.10}$	84.1 / 96.7 $\pm$ 11.4	⋯
Swift-XRT	00015096002	2022-09-01	59823.5	4.8	1.54 ± 0.20	$0.78^{+0.15}_{-0.13}$	50.49 / 68.5 $\pm$ 9.3	⋯
	00015096003	2023-03-04	60007.0	2.9	1.29 ± 0.15	$0.88^{+0.14}_{-0.12}$	96.4 / 108.4 $\pm$ 12.1	⋯
	00015096004	2023-03-05	60008.3	4.9				
	0111260201	2002-05-11	52405.6	9.3 (pn)	1.53 ± 0.04	0.553 ± 0.022	829.3 / 893.9 $\pm$ 39.0	0.97 ± 0.06 (MOS2)
XMM-Newton				12.1 (MOS2)				
	0910390101	2022-02-08	59618.1	58.7 (pn)	1.481 ± 0.012	0.786 ± 0.011	2729.1 / 2789.1 $\pm$ 73.6	1.003 ± 0.020 (MOS1)
				80.12 (MOS1)				$1.010^{+0.020}_{-0.019}$ (MOS2)
				81.1 (MOS2)				
NuSTAR + Swift-XRT	60201013002	2017-04-30	57873.2	36.9 (FPMA)	1.12 ± 0.07	$3.438^{+0.345}_{-0.001}$	885.9 / 943.5 $\pm$ 38.3	0.97 ± 0.08 (FPMB)
				36.8 (FPMB)				$0.27^{+0.07}_{-0.06}$ (XRT)

Note. For Swift-XRT and XMM-Newton, the flux is given for an energy range of 0.5–10 keV, while the flux measured with NuSTAR and Swift-XRT simultaneously is given for the range 0.5–80 keV.
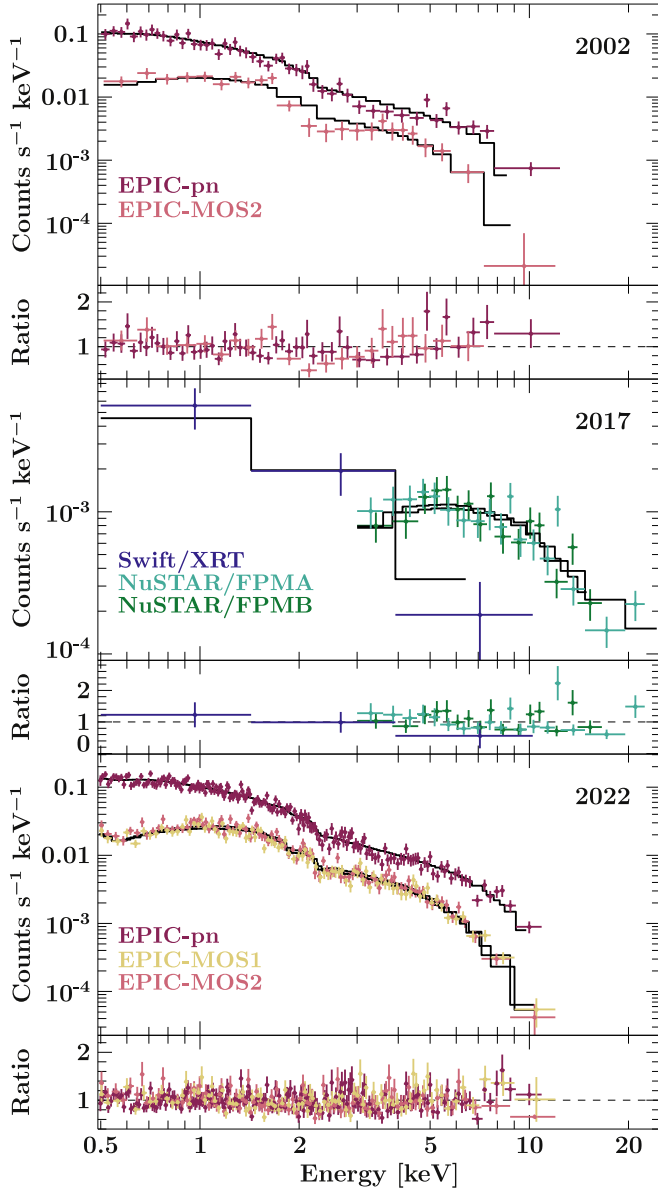
Figure 2. Simultaneous X-ray spectra taken in 2002 (top) and 2022 (bottom) with XMM-Newton, and in 2017 with Swift/XRT and NuSTAR (middle), including ratios of the spectral bins vs. the best-fit model.

Figure 3. XMM light curve in 1 ks binning and for different energy bands (top: 0.3–10 keV, middle: 0.3–2 keV, and bottom: 2–10 keV). Shaded parts of the light curves mark the times in which background flaring affected the light curve in the full and hard energy ranges, and these times are excluded in our computation of the $\sigma_{\rm rms}^2$ values.

Table 4
Normalized Excess Variance in X-Ray (1 ks Binning) as Observed with XMM-Newton and in Several Gigahertz Radio Bands with the 100 m Effelsberg Telescope

X-Ray		
Energy Band	$\sigma_{\rm RMS}^2$ (10^{-2})	Bins
0.3–10 keV	0.10 ± 0.07	73
0.3–2 keV	0.27 ± 0.12	83
2–10 keV	0.16 ± 0.2	71
Radio		
Wavelength	$\sigma_{\rm RMS}^2$ [10^{-2}]	Bins
60 mm	-0.03 ± 0.03	14
20 mm	0.06 ± 0.05	16
14 mm	-0.13 ± 0.21	17
7 mm	-1.6 ± 1.8	10
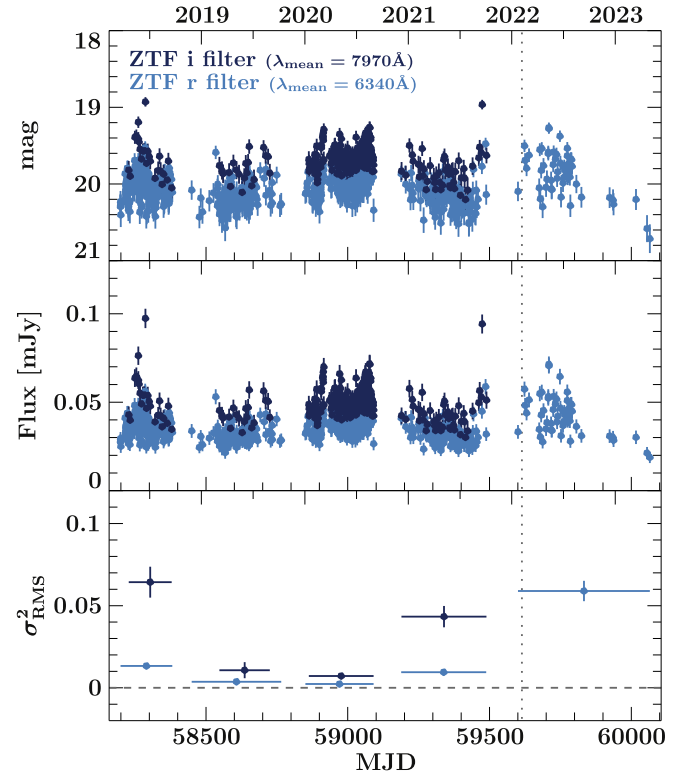
Figure 4. Optical long-term light curves in the *r* and *i* bands from data taken with ZTF: light curves in magnitudes (top), light curves in units of mJy (middle), and normalized excess variance $\sigma_{\rm RMS}^2$ for each epoch covering a time range of roughly 10 months (bottom). The dotted line marks the time of the flare detection at γ-ray energies. The dashed line in the bottom panel indicates $\sigma_{\rm RMS}^2 = 0$.

(The data used to create this figure are available in the online article.)
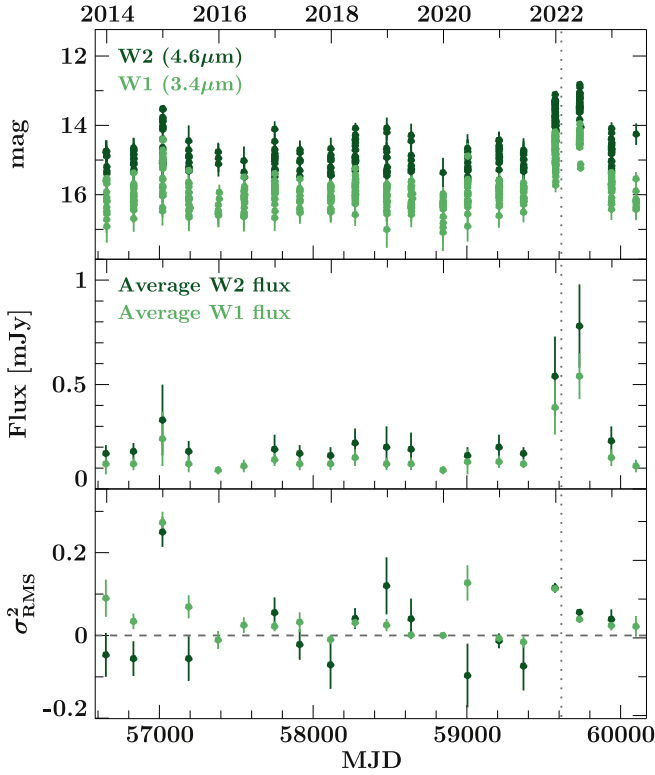
Figure 5. IR light curves for the W1 and W2 bands taken with NEOWISE: light curves showing all data points (top), and the average fluxes (middle) and normalized excess variance σ_{RMS}^2 (bottom) for each epoch from 2014 until 2023. The dotted line marks the time of the flare detection at γ-ray energies. The dashed line in the bottom panel indicates $\sigma_{\mathrm{RMS}}^2 = 0$.

(The data used to create this figure are available in the online article.)

gradually declines back to the baseline levels. A similar behavior is observed in the optical data (Figure 4).

4.3.3. Long-term Variability in the Radio Band

The radio data taken with the 100 m Effelsberg telescope (light curve shown in Figure 1) have an average monitoring cadence of 3 to 5 weeks, depending on the observing frequency. For none of the radio bands do we find σ_{RMS}^2 that is significantly above the expected noise level (see Table 4).

Interestingly, the polarization at 60 mm is more variable, but also higher than at 20 mm for the time range of at least 3 months before mid-2022. After that, the polarization in both bands is roughly the same apart from a dip in the 60 mm band at MJD 59780. Similarly, the EVPA at 60 mm is rotating significantly more than the EVPA measured at 20 mm.

4.4. Spectral Energy Distribution Modeling

The broadband SEDs in the quiescent and flaring states are well described by the steady-state leptonic model of Böttcher et al. (2013). It is a one-zone model, assuming a spherical emission region with radius R_b, located at a distance d from the central SMBH, moving along the jet with bulk Lorentz factor Γ, resulting in relativistic Doppler boosting of electromagnetic radiation by a Doppler factor $\delta = (\Gamma[1 - \beta_\Gamma \cos\theta_{\mathrm{obs}}])^{-1}$, where β_Γ is the normalized velocity corresponding to the Lorentz factor Γ, and θ_{obs} is the angle between the jet axis and our line of sight, chosen to be $\theta_{\mathrm{obs}} = 1/\Gamma$ in order to reduce the number of free parameters. The code evaluates a

self-consistent equilibrium electron distribution, based on a rapid acceleration process, injecting a power-law distribution of electrons with index q between a minimum and maximum electron Lorentz factor $\gamma_{\mathrm{min/max}}$. This injection is self-consistently balanced with radiative energy losses and escape from the emission region on an escape timescale $t_{\mathrm{esc}} = \eta_{\mathrm{esc}} R/c$, parameterized by an escape timescale parameter $\eta_{\mathrm{esc}} \geqslant 1$. The resulting electron population with density spectrum $n_e(\gamma)$ in the comoving frame of the emission region carries a power of $L_e = \pi R_b^2 \Gamma^2 \beta_\Gamma m_e c^3 \int d\gamma \gamma n_e(\gamma)$ along the jet. Radiation mechanisms included are synchrotron radiation in a tangled magnetic field of strength B, synchrotron self-Compton (SSC), and external Compton (EC) scattering of both the direct accretion-disk radiation, EC (disk), and an external blackbody radiation field (temperature T_{DT} and radiation energy density u_{DT}), assumed to be isotropic in the AGN rest frame, representative of IR emission from warm dust from the dust torus (DT), EC (DT). For each model simulation, the code evaluates, in addition to the electron power mentioned above, the power carried in the magnetic field (Poynting flux), $L_B = \pi R_b^2 \Gamma^2 \beta_\Gamma c(B^2/8\pi)$, and the energy partition ratio, $\epsilon_{Be} = L_B/L_e$. A set of model parameters describing the quiescent and flaring SEDs shown in Figure 6 are listed in Table 5. The chosen solutions are not necessarily unique given the significant degeneracies in the model.

Figure 6 illustrates that the SEDs in both states can be well represented with this model, with the high-energy (X-ray through γ-ray) emission having significant contributions from both EC (disk) and EC (DT), while SSC is subdominant. The change from the quiescent to the flaring state is achieved primarily through a harder injection spectral index of the electron spectrum and a higher γ_{min}, indicating an increased electron acceleration efficiency. The optical emission, in our model fits, is dominated by the thermal accretion-disk radiation in the quiescent state, in agreement with the very low degree of polarization measured by the Steward Observatory (also in the quiescent state, although not contemporaneous with our high-energy observations). In the flaring state, the much harder electron synchrotron spectrum dominates the optical emission. One would therefore expect significant optical polarization in this state, if the magnetic field is at least partially ordered in the emission region. Future polarimetric measurements during flaring states should be able to test this hypothesis.

We note that the jet plasma, especially in the flaring state, is out of equipartition, and is dominated by Poynting flux, with the chosen model parameters. The magnetic field values are also higher by a factor of a few compared to the estimates of Benke et al. (2024) for the 43 GHz core (0.8 and 1.7 G, depending on the equipartition assumptions). This is consistent with the expectation that the high-energy emission region is located closer to the central engine than the 43 GHz core, as our model configuration for the high-energy emission region is still optically thick at radio frequencies. This is, however, inconsistent with the estimated distance of 0.32 ± 0.02 pc for the 43 GHz core. As there are significant degeneracies in our model parameters, a similarly adequate fit with a smaller value of d could remedy this discrepancy (e.g., a smaller distance accompanied by an increased magnetic field). On the other hand, the estimate of the radio-core distance relied on the core-shift measurement under the assumption of a conical jet profile, and on the uncertain viewing angle. A nonconical jet profile
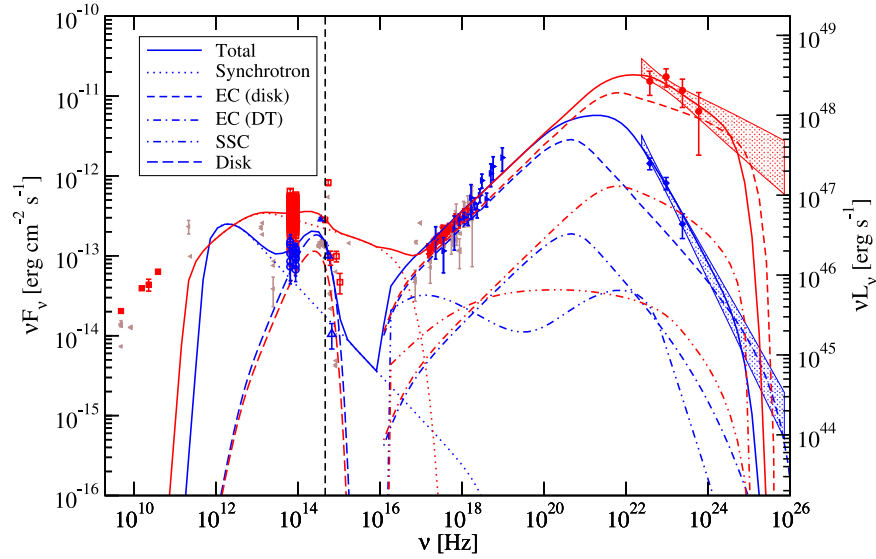
Figure 6. Broadband SED of TXS 1508+572 in the quiescent state (blue) and during the 2022 flare (red). Archival data are taken from the online SED Builder (https://tools.ssdc.asi.it/SED/) provided by the Space Science Data Center, and shown via gray data points. Optical data from SARA taken during the quiescent state are taken from Marcotulli et al. (2020). The dashed vertical line indicates the frequency of the redshifted Lyα line. The model fits are produced with the code of Böttcher et al. (2013), using the parameters listed in Table 5.
(The data used to create this figure are available in the online article.)

Table 5
Spectral Energy Distribution Model Fit Parameters Used for the Modeling Shown in Figure 6

Parameter	Quiescent	Flare
L_e [erg s^{-1}]	5.6×10^{45}	2.7×10^{45}
$\gamma_{\min}$	150	450
$\gamma_{\max}$	2.0×10^5	3.0×10^4
q	3.1	2.3
B [G]	5.0	2.8
$\eta_{\rm esc}$	10	10
d [pc]	0.4	0.35
Γ	20	20
$L_{\rm disk}$ [erg s^{-1}]	4.0×10^{47}	2.5×10^{47}
R_b [cm]	1.3×10^{16}	4.0×10^{16}
$M_{\rm BH}$ [M$_\odot$]	1.5×10^{10}	1.5×10^{10}
$T_{\rm DT}$ [K]	1.0×10^3	1.0×10^3
$u_{\rm DT}$ [erg cm^{-3}]	5.0×10^{-4}	5.0×10^{-4}
L_B [erg s^{-1}]	6.3×10^{45}	1.9×10^{46}
ϵ_{Be}	1.1	7.0

and/or different viewing angle would obviously yield different values for the radio-core distance.

5. Discussion

5.1. γ-Ray Luminosity of the Flare

During the quiescent state, the γ-ray luminosity of TXS 1508 +572 is 2.8×10^{48} erg s^{-1}, comparable to other $z > 3$ Fermi-LAT-detected blazars (Ackermann et al. 2017). During the flaring state, which lasted for longer than 6 months in 2022 with two peak times in February and August, respectively, the γ-ray luminosity increases to $>5 \times 10^{49}$ erg s^{-1}, making this flare by TXS 1508+572 one of the most luminous that Fermi-LAT has ever detected. Only two blazars, B3 1343+451 and CTA 102, exhibited flares with an isotropic γ-ray luminosity $> 10^{50}$ erg s^{-1} (Gasparyan et al. 2018; Sahakyan

et al. 2020). A few others have shown peak flare luminosities $> 10^{49}$ erg s^{-1}: 3C 454.3 (Nalewajko 2013, 2017), 3C 279 (Ackermann et al. 2016), PKS 0402−362 (Nalewajko 2017), and PKS 0537−286 (Sahakyan et al. 2020). Among those, B3 1343+451 and PKS 0537-286 are also high-z objects with $z = 2.53$ and $z = 3.01$, respectively, showing that blazars in the early Universe are able to produce equally luminous flares; and given that three out of seven of the most extreme flares have been observed for these distant sources hints at those luminous flares being more common in high-z blazars.

5.2. Comparison of Different Broadband Spectral Energy Distribution Modeling

The quiescent SED of TXS 1508+572 has been modeled by Ackermann et al. (2017) using nonsimultaneous data and by Marcotulli et al. (2020) using a data set with simultaneous optical and X-ray data. All models use a one-zone leptonic model considering both SSC and EC radiation for the high-energy component, and in all cases EC dominates the X-ray and γ-ray emission. The SEDs in Ackermann et al. (2017) and Marcotulli et al. (2020) include thermal emission from the dust torus even though it is not directly constrained by observational data in the IR band. Our model does include potential radiation from the dust torus as a seed photon field for the EC component, but we find that EC radiation from the accretion disk strongly dominates the high-energy emission.

Our SED modeling approach differs from that of Ackermann et al. (2017) and Marcotulli et al. (2020) in that we attempt to simultaneously describe the quiescent and flaring states of TXS 1508+572 while changing only a small subset of model parameters. Spectroscopic estimates of the black hole mass of TXS 1508+572 are in the range $M_{\rm BH} = 3\text{–}8 \times 10^8\ M_\odot$ (Ackermann et al. 2017; Diana et al. 2022). A standard Shakura–Sunyaev accretion disk (Shakura & Sunyaev 1973) corresponding to the estimated $M_{\rm BH}$ values is too hot to provide the low frequency seed photons that our model favors for the

origin of the high-energy SED component via the EC (disk) process. Given that the temperature-dependent peak frequency of the disk emission is $\nu_{\text{peak}} \propto M^{-1/4}$, our model assuming a Shakura–Sunyaev disk favors a larger black hole mass of $M = 1.5 \times 10^{10}\ M_\odot$. This discrepancy is in line with quasar spectra tending to show ionization states compatible with disk temperatures lower than predicted in the standard Shakura–Sunyaev theory (Bonning et al. 2013). In addition, the spin of the black hole will also have an impact on the geometry and temperature profile of the disk, which is not taken into account in our SED model. In particular, a retrograde spin would push the innermost stable circular orbit to larger distances compared to a Schwarzschild black hole (Bardeen et al. 1972), with the effect of also lowering the effective disk temperature.

The magnetic field values favored by our SED model are also higher than those in Ackermann et al. (2017) and Marcotulli et al. (2020), and we find a higher bulk Lorentz factor ($\Gamma = 20$ instead of $\Gamma = 11$) as well as higher γ_{min} and γ_{max} values that are expected if the electron acceleration efficiency increases during a γ-ray flare. The measurement of superluminal speeds $> 15c$ with our VLBI monitoring campaign (Benke et al. 2024) supports our higher value of Γ. The distance of the dissipation region from the central engine is further away than described by Ackermann et al. (2017), but at a similar distance as determined by Marcotulli et al. (2020). Earlier works by Sikora et al. (2009) and Ghisellini & Tavecchio (2009) argue that such a large distance favors EC emission from the broad-line region or the dusty torus instead of the accretion disk due to the decrease of the energy density of disk photons and less favorable scattering geometry with increasing distance. Nonetheless, there exists currently almost no constraining information about the properties of the broad-line region or the torus, and we have assumed a relatively low energy density of the isotropic external radiation field from the latter, when compared to the standard scaling relations presented in Ghisellini & Tavecchio (2009). In addition, the luminosity of the accretion disk of TXS 1508+572 exceeds 10^{47} erg s^{-1}, and we assume a substantially larger black hole mass than what the estimates by Sikora et al. (2009) and Ghisellini & Tavecchio (2009) were based on. Due to this larger black hole mass, the disk truncates and extends out to larger radii, so that IC scattering can occur under more favorable interaction angles than in the case of smaller black hole masses. The code by Böttcher et al. (2013), which is used for our modeling, takes into account the full angle dependence of the IC scattering of disk photons.

5.3. Multiwavelength Variability

By computing the σ_{RMS}^2 value for each energy band for which we have monitoring data available, albeit covering different timescales, we can compare the variability of the source at different wavelengths. While at X-ray energies we see only a small amount of variability within 1 day, the IR σ_{RMS}^2 values for some epochs indicate more significant variability for time ranges that cover a few days at most. For blazars in general, the variability of IR emission seems to be correlated with the presence of γ-ray emission (Mao et al. 2018). The variability of TXS 1508+572 in the optical and IR regime seems to precede the γ-ray activity given that already before the detection of the γ-ray flare the IR flux and the intraday variability had increased. Considering that TXS 1508+572 would be classified as a low-synchrotron-peaked (LSP) source
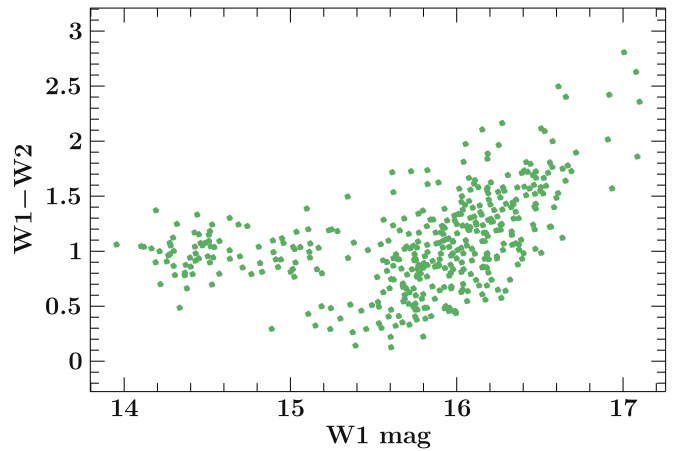
Figure 7. Change of the W1 − W2 color with respect to the brightness of the W1 band.

(in the source frame), the variability displayed at IR wavelengths would occur in the R band for a source at $z = 0$. Paliya et al. (2017) found that LSP blazars are more variable on intranight timescales, and for which the commonly accepted scenario is that this variability originates from the nonthermal emission of the jet. Therefore, we suggest that the observed variability is connected to synchrotron emission from the jet rather than being a signature from the accretion disk.

We look at possible correlations between the brightness versus a color change, and find none at optical wavelengths. This behavior is not unusual though, as the majority of FSRQs exhibit neither a redder-when-brighter or bluer-when-brighter trend (Negi et al. 2022). In order to assess the change of the IR W1 − W2 color with the IR brightness of TXS 1508+572, we plot the W1 − W2 color over the W1 magnitude for all NEOWISE data taken simultaneously in Figure 7. The IR flux from TXS 1508+572 shows a bluer-when-brighter behavior at low fluxes and transitions to a state with no color change for $m_{\text{W1}} < 15$, which could indicate the transition between a disk-dominated and synchrotron-dominated IR flux. Indeed, the bluer-when-brighter trend of IR emission has been observed with NEOWISE for the majority of both FSRQs and BL Lac objects (Anjum et al. 2020).

5.4. Radio Very Long Baseline Interferometry Campaign and Polarization

Benke et al. (2024) present the results from a VLBI monitoring campaign triggered by the γ-ray flare of TXS 1508+572 in 2022. The VLBA and the Effelsberg 100 m radio telescope were used to obtain milliarcsecond-scale images at 15, 22, and 43 GHz. In addition, one observation at 86 GHz was performed with the VLBA and the Green Bank Telescope, allowing them to probe the jet of TXS 1508+572 at 456 GHz in the rest-frame frequency of the source. In general, the radio observations support the underlying scenario in which the injection of fresh electrons in the acceleration zone explains the observed broadband variability. By tracking the evolution of the jet over a time range of roughly 10 months, Benke et al. (2024) find morphological changes in the jet and apparent superluminal speeds of the jet component motion of $\sim 14c$–$32c$, depending on frequency. The latter is in agreement with the bulk Lorentz factor of $\Gamma = 20$ that is favored by our SED model. The observed jet components can be traced back to an
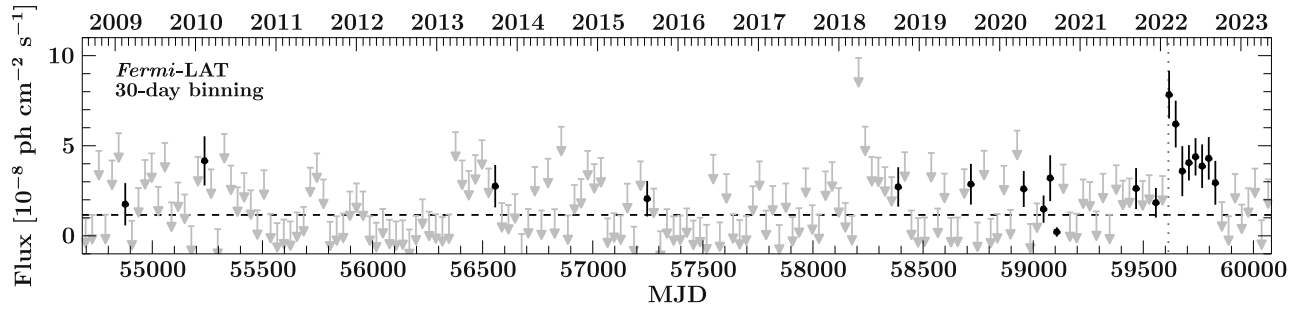
Figure 8. Long-term Fermi-LAT light curve of TXS 1508+572 in 30 day binning. Bins with TS < 9 are plotted as arrows at the 2σ upper limit. The dashed horizontal line marks the long-term average flux, while the dotted vertical line marks the flare detection in 2022.

ejection time between 2016 and 2019, and would not be causally connected to the γ-ray activity seen in 2022. When computing the 30 day binned light curve for TXS 1508+572 over the entire duration of the Fermi mission (see Figure 8), we find several times when the signal from the blazar is TS $\geqslant 9$ ($\gtrsim 3\sigma$), with four bins falling into the year 2020, which indicates enhanced activity of the source during that time range. Assuming that the γ-ray flare in the first half of 2022 has produced a new outflowing component, we expect to detect a new radio component to be resolvable by VLBI between 2025 and 2027.

While the VLBI radio observations spatially resolve the jet within the inner several parsecs of the source, the radio core itself likely consists of multiple emission zones that cannot be resolved. Radio polarization measurements at different frequencies from the Effelsberg observatory allow us to look into the structure of the unresolved radio core. The Effelsberg data (Figure 1) show that the time variability of the polarization degree is more pronounced than the Stokes I variability, especially at 60 mm, indicating that the core itself consists of several emission regions.

VLBI polarization measurements of TXS 1508+572 have been analyzed by O'Sullivan et al. (2011), who reported the detection of polarization at 60 mm and 36 mm for the core, and at 60 mm for a single jet component. Unfortunately, our VLBI observations do not fall into a time when the 60 mm net polarization is higher than the net polarization at 20 mm, and without synchronous data, interpretation of the apparent short timescale variability of the polarization parameters from MJD 59680 to MJD 59750 (see Figure 1) would be too speculative.

6. Conclusions

The detection of a γ-ray flare by a $z > 3$ blazar is rare: PKS 0537−286 is the only source which has shown multiple flares, which were so bright that they could be detected on daily timescales (Sahakyan et al. 2023), and which has been communicated in real time by the LAT collaboration (Cheung 2017; Angioni 2020; Valverde & Forman 2022). The study by Kreter et al. (2020) finds nine TS $\geqslant 25$ detections for three $z > 3$ blazars (excluding PKS 0537−286) over a time span of 10 yr and 8 months, resulting in a high-z blazar flare every 14 months on average.

The 2022 flare from TXS 1508+572 reported in this paper is among the most luminous events that have been seen from this source class. For both the quiescent and the flaring state, the broadband SED model for TXS 1508+572 requires a dominant contribution from EC emission to describe the high-energy emission, similar to FSRQs in the local Universe displaying

Compton dominance at all activity states (e.g., Krauß et al. 2016). Our SED modeling suggests a lower accretion-disk temperature than expected in a Shakura–Sunyev disk, as well as a high bulk Lorentz factor of $\Gamma = 20$ that is in line with the superluminal motion in the jet of TXS 1508+572 described in Benke et al. (2024). At present, the data covering most of the synchrotron component are sparse, and a significant portion of optical information that could help constrain the emission from the accretion disk is lost due Lyα absorption.

Hence, constraining the low-energy component of the SED of TXS 1508+572, or for any blazar with $z > 3$ for that matter, presents a challenge. The low observed optical polarization during a quiescent state allows us to conclude that the optical emission from TXS 1508+572 is strongly dominated by thermal radiation from the accretion disk. However, we were not able to obtain an optical polarization measurement during the flaring state. Similar to local FSRQs, TXS 1508+572 also presents variability from the jet emission, which is measured in the IR band. While only a small number of such systems have been studied so far, current hard X-ray band and future MeV missions, such as the Compton Spectrometer and Imager (Tomsick et al. 2019, 2023), or the Advanced Particle-astrophysics Telescope (Buckley et al. 2019, 2022), are ideal to search for these distant objects, and their enhanced sensitivity promises more detections of powerful sources in the early Universe in coming years.

ORCID iDs

Andrea Gokus ⬡ https://orcid.org/0000-0002-5726-5216
Markus Böttcher ⬡ https://orcid.org/0000-0002-8434-5692
Manel Errando ⬡ https://orcid.org/0000-0002-1853-863X
Michael Kreter ⬡ https://orcid.org/0000-0002-3092-3506
Jonas Heßdörfer ⬡ https://orcid.org/0009-0009-7841-1065
Florian Eppel ⬡ https://orcid.org/0000-0001-7112-9942
Matthias Kadler ⬡ https://orcid.org/0000-0001-5606-6154
Paul S. Smith ⬡ https://orcid.org/0000-0002-5083-3663
Petra Benke ⬡ https://orcid.org/0009-0006-4186-9978
Leonid I. Gurvits ⬡ https://orcid.org/0000-0002-0694-2459
Alex Kraus ⬡ https://orcid.org/0000-0002-4184-9372
Mikhail Lisakov ⬡ https://orcid.org/0000-0001-6088-3819
Felicia McBride ⬡ https://orcid.org/0000-0001-6191-1244
Eduardo Ros ⬡ https://orcid.org/0000-0001-9503-4892
Florian Rösch ⬡ https://orcid.org/0009-0000-4620-2458
Jörn Wilms ⬡ https://orcid.org/0000-0003-2065-5410

References

Abdollahi, S., Acero, F., Ackermann, M., et al. 2020, ApJS, 247, 33
Ackermann, M., Ajello, M., Baldini, L., et al. 2017, ApJL, 837, L5
Ackermann, M., Anantua, R., Asano, K., et al. 2016, ApJL, 824, L20
Aharonian, F. A. 2000, NewA, 5, 377
Aharonian, F. A. 2002, MNRAS, 332, 215
Ajello, M., Angioni, R., Axelsson, M., et al. 2020, ApJ, 892, 105
Ajello, M., Baldini, L., Ballet, J., et al. 2022, ApJS, 263, 24
Alexander, T., & Natarajan, P. 2014, Sci, 345, 1330
Angioni, R. 2020, ATel, 14285, 1
Anjum, A., Stalin, C. S., Rakshit, S., Gudennavar, S. B., & Durgapal, A. 2020, MNRAS, 494, 764
Atwood, W. B., Abdo, A. A., Ackermann, M., et al. 2009, ApJ, 697, 1071
Bardeen, J. M., Press, W. H., & Teukolsky, S. A. 1972, ApJ, 178, 347
Begelman, M. C., Volonteri, M., & Rees, M. J. 2006, 370, 289
Belladitta, S., Caccianiga, A., Diana, A., et al. 2022, A&A, 660, A74
Belladitta, S., Moretti, A., Caccianiga, A., et al. 2020, A&A, 635, L7
Bellm, E. C., Kulkarni, S. R., Graham, M. J., et al. 2019, PASP, 131, 018002
Benke, P., Gokus, A., Lisakov, M., et al. 2024, A&A, 689, A43
Blandford, R. D., & Levinson, A. 1995, ApJ, 441, 79
Błażejowski, M., Sikora, M., Moderski, R., & Madejski, G. M. 2000, ApJ, 545, 107
Bloemen, H., Bennett, K., Blom, J. J., et al. 1995, A&A, 293, L1
Bloom, S. D., & Marscher, A. P. 1996, ApJ, 461, 657
Boettcher, M., & Schlickeiser, R. 1997, A&A, 325, 866
Bonning, E. W., Shields, G. A., Stevens, A. C., & Salviander, S. 2013, ApJ, 770, 30
Böttcher, M., Reimer, A., Sweeney, K., & Prakash, A. 2013, ApJ, 768, 54
Buckley, J., Adapt, Alnussirat, S., et al. 2022, in ICRC (Berlin), 37, 655
Buckley, J., Bergstrom, L., Binns, B., et al. 2019, BAAS, 51, 78
Burke, C. J., Liu, X., & Shen, Y. 2024, MNRAS, 527, 5356
Cash, W. 1979, ApJ, 228, 939
Cheung, C. C. 2004, ApJL, 600, L23
Cheung, C. C. 2017, ATel, 10356, 1
Dermer, C. D., & Schlickeiser, R. 1993, ApJ, 416, 458
Diana, A., Caccianiga, A., Ighina, L., et al. 2022, MNRAS, 511, 5436
Domínguez, A., Østergaard Kirkeberg, P., Wojtak, R., et al. 2024, MNRAS, 527, 4632
Eppel, F., Kadler, M., Heßdörfer, J., et al. 2024, A&A, 684, A11
Frey, S., Gurvits, L. I., Kellermann, K. I., Schilizzi, R. T., & Pauliny-Toth, I. I. K. 1997, A&A, 325, 511
Gasparyan, S., Sahakyan, N., Baghmanyan, V., & Zargaryan, D. 2018, ApJ, 863, 114
Gehrels, N., Chincarini, G., Giommi, P., et al. 2004, ApJ, 611, 1005
Ghisellini, G., Della Ceca, R., Volonteri, M., et al. 2010, 405, 387
Ghisellini, G., Haardt, F., Della Ceca, R., Volonteri, M., & Sbarrato, T. 2013, MNRAS, 432, 2818
Ghisellini, G., & Tavecchio, F. 2009, MNRAS, 397, 985
Gokus, A., Kreter, M., Kadler, M., et al. 2022, ATel, 15202, 1
Gunn, J. E., & Peterson, B. A. 1965, ApJ, 142, 1633
HI4PI Collaboration, Ben Bekhti, N., Flöer, L., et al. 2016, A&A, 594, A116
Hook, I. M., McMahon, R. G., Patnaik, A. R., et al. 1995, MNRAS, 273, L63
Houck, J. C., & Denicola, L. A. 2000, in ASP Conf. Ser. 21, Astronomical Data Analysis Software and Systems IX, ed. N. Manset, C. Veillet, & D. Crabtree, 591 (San Francisco, CA: ASP)
Inayoshi, K., Visbal, E., & Haiman, Z. 2020, ARA&A, 58, 27
IRSA 2022, Zwicky Transient Facility Image Service, IPAC, doi:10.26131/IRSA539
Jansen, F., Lumb, D., Altieri, B., et al. 2001, A&A, 365, L1
Johnson, J. L., & Haardt, F. 2016, PASA, 33, e007
Kappes, A., Burd, P. R., Kadler, M., et al. 2022, A&A, 663, A44
Krauß, F., Wilms, J., Kadler, M., et al. 2016, A&A, 591, A130
Kreter, M., Gokus, A., Krauss, F., et al. 2020, ApJ, 903, 128
Lai, S., Onken, C. A., Wolf, C., Bian, F., & Fan, X. 2024, MNRAS, 531, 2245
Li, S., Xia, Z.-Q., Liang, Y.-F., Liao, N.-H., & Fan, Y.-Z. 2018, ApJ, 853, 159
Liao, N.-H., Dou, L.-M., Jiang, N., et al. 2019, ApJL, 879, L9
Liao, N.-H., Li, S., & Fan, Y.-Z. 2018, ApJL, 865, L17
Liao, N.-H., Li, S., Sheng, Z.-F., & Fan, Y.-Z. 2020, ApJL, 898, L56
Lobanov, A. P., Gurvits, L. I., Frey, S., et al. 2001, ApJ, 547, 714
Madau, P., & Rees, M. J. 2001, ApJ, 551, L27
Mainzer, A., Bauer, J., Cutri, R. M., et al. 2014, ApJ, 792, 30
Mannheim, K. 1993, A&A, 269, 67
Mannheim, K., & Biermann, P. L. 1992, A&A, 253, L21
Mao, L., Zhang, X., & Yi, T. 2018, Ap&SS, 363, 167
Maraschi, L., Ghisellini, G., & Celotti, A. 1992, ApJL, 397, L5
Marcotulli, L., Paliya, V., Ajello, M., et al. 2020, ApJ, 889, 164
Masci, F. J., Laher, R. R., Rusholme, B., et al. 2019, PASP, 131, 018003
Massaro, E., Giommi, P., Leto, C., et al. 2009, A&A, 495, 691
Massaro, E., Maselli, A., Leto, C., et al. 2015, Ap&SS, 357, 75
Mathur, S., & Elvis, M. 1995, AJ, 110, 1551
Mattox, J. R., Bertsch, D. L., Chiang, J., et al. 1996, ApJ, 461, 396
McKinney, J. C., Tchekhovskoy, A., Sadowski, A., & Narayan, R. 2014, MNRAS, 441, 3177
Medvedev, P., Sazonov, S., Gilfanov, M., et al. 2020, MNRAS, 497, 1842
Migliori, G., Siemiginowska, A., Sobolewska, M., et al. 2023, MNRAS, 524, 1087
Moran, E. C., & Helfand, D. J. 1997, ApJL, 484, L95
Mücke, A., & Protheroe, R. J. 2001, APh, 15, 121
Mücke, A., Protheroe, R. J., Engel, R., Rachen, J. P., & Stanev, T. 2003, APh, 18, 593
Nalewajko, K. 2013, MNRAS, 430, 1324
Nalewajko, K. 2017, Galax, 5, 100

Nandra, K., George, I. M., Mushotzky, R. F., Turner, T. J., & Yaqoob, T. 1997, ApJ, 476, 70

Negi, V., Joshi, R., Chand, K., et al. 2022, MNRAS, 510, 1791

NEOWISE Team 2020, NEOWISE-R Single Exposure (L1b) Source Table, IPAC, doi:10.26131/IRSA144

Orienti, M., D'Ammando, F., Giroletti, M., et al. 2014, MNRAS, 444, 3040

O'Sullivan, S. P., Gabuzda, D. C., & Gurvits, L. I. 2011, MNRAS, 415, 3049

Paliya, V. S., Ajello, M., Ojha, R., et al. 2019, ApJ, 871, 211

Paliya, V. S., Parker, M. L., Fabian, A. C., & Stalin, C. S. 2016, ApJ, 825, 74

Paliya, V. S., Stalin, C. S., Ajello, M., & Kaur, A. 2017, ApJ, 844, 32

Planck Collaboration, Ade, P. A. R., Aghanim, N., et al. 2016, A&A, 594, A13

Rakshit, S., Johnson, A., Stalin, C. S., Gandhi, P., & Hoenig, S. 2019, MNRAS, 483, 2362

Sądowski, A., Narayan, R., McKinney, J. C., & Tchekhovskoy, A. 2014, MNRAS, 439, 503

Sahakyan, N., Harutyunyan, G., & Israyelyan, D. 2023, MNRAS, 521, 1013

Sahakyan, N., Israyelyan, D., Harutyunyan, G., Khachatryan, M., & Gasparyan, S. 2020, MNRAS, 498, 2594

Sbarrato, T., Ghisellini, G., Tagliaferri, G., et al. 2015, MNRAS, 446, 2483

Sbarrato, T., Ghisellini, G., Tagliaferri, G., et al. 2022, A&A, 663, A147

Schmidt, G. D., Stockman, H. S., & Smith, P. S. 1992, ApJL, 398, L57

Schneider, D. P., Hall, P. B., Richards, G. T., et al. 2007, AJ, 134, 102

Shakura, N. I., & Sunyaev, R. A. 1973, A&A, 24, 337

Siemiginowska, A., Smith, R. K., Aldcroft, T. L., et al. 2003, ApJL, 598, L15

Sikora, M., Begelman, M. C., & Rees, M. J. 1994, ApJ, 421, 153

Sikora, M., Błażejowski, M., Moderski, R., & Madejski, G. M. 2002, ApJ, 577, 78

Sikora, M., Stawarz, Ł., Moderski, R., Nalewajko, K., & Madejski, G. M. 2009, ApJ, 704, 38

Smith, P. S., Williams, G. G., Schmidt, G. D., Diamond-Stanic, A. M., & Means, D. L. 2007, ApJ, 663, 118

Strüder, L., Briel, U., Dennerl, K., et al. 2001, A&A, 365, L18

Titov, O., Frey, S., Melnikov, A., et al. 2023, AJ, 165, 69

Tomsick, J., Zoglauer, A., Sleator, C., et al. 2019, BAAS, 51, 98

Tomsick, J. A., Boggs, S. E., Zoglauer, A., et al. 2023, arXiv:2308.12362

Turner, M. J. L., Abbey, A., Arnaud, M., et al. 2001, A&A, 365, L27

Urry, C. M., & Padovani, P. 1995, PASP, 107, 803

Valverde, J., & Forman, J. 2022, ATel, 15405, 1

Verner, D. A., Ferland, G. J., Korista, K. T., & Yakovlev, D. G. 1996, ApJ, 465, 487

Volonteri, M., Haardt, F., Ghisellini, G., & Della Ceca, R. 2011, MNRAS, 416, 216

Wang, F., Yang, J., Fan, X., et al. 2021, ApJL, 907, L1

Wilms, J., Allen, A., & McCray, R. 2000, ApJ, 542, 914

Wood, M., Caputo, R., Charles, E., et al. 2017, in ICRC (Busan), 301, 824

Yuan, W., Fabian, A. C., Celotti, A., & Jonker, P. G. 2003, MNRAS, 346, L7